

ARTICLE

Open Access

Ultra-sensitive ethanol detection using a chemiresistive SnO_2 thin-film gas sensor functionalized with RuO_2 nanosheets

Wonkeun Park¹, Yunsung Kang², Xiaoyan Jin³, Dongseok Lee¹ , Seong-Ju Hwang⁴  and Jongbaeg Kim¹ 

Abstract

This study presents the design and fabrication of a ruthenium dioxide (RuO_2) nanosheets-functionalized tin dioxide (SnO_2) thin-film gas sensor integrated with a microheater in a suspended membrane structure. The RuO_2 nanosheets are synthesized via an intercalation-driven exfoliation process and subsequently deposited onto a sputtered SnO_2 thin film. Due to the catalytic properties and high surface-to-volume ratio of RuO_2 nanosheets, the functionalized sensor demonstrates a 337% increase in response ($R_{\text{air}}/R_{\text{gas}}$) to 10 ppm ethanol compared to pristine SnO_2 thin film. The sensor achieves sensitive detection from a few parts-per-million (ppm) down to several parts-per-billion (ppb) concentrations of ethanol. Evaluations under varied humidity conditions, as well as selectivity and 28-day stability tests, demonstrate that the RuO_2 nanosheets-functionalized sensor maintains reliable performance. These results highlight its potential as a sensitive, selective, and low-power solution for ethanol gas detection. Furthermore, the sensor successfully tracks breath alcohol concentration in real-time through controlled alcohol intake experiments, demonstrating its feasibility for practical breath alcohol detection.

Introduction

The detection of volatile organic compounds (VOCs) in daily life and industrial environments has garnered significant attention over the past decades. VOCs include benzene, toluene, ethylene, xylene (often referred to as BTEX), formaldehyde, acetone, and ethanol, which are known to have harmful effects on both the environment and human health^{1–3}. Among these, ethanol is a colorless organic compound, commonly referred to as alcohol or ethyl alcohol, that is widely utilized across various fields such as chemical, food, industrial, medical, and agricultural products^{4–6}. Despite its broad applicability, ethanol is highly flammable at elevated temperatures and

exhibits combustible characteristics upon exposure to oxidants^{7,8}. Furthermore, excessive exposure to ethanol gas can adversely affect the neurovascular system, vision, and respiratory system⁹. The U.S. Occupational Safety and Health Administration recommends a maximum ethanol exposure limit of 1000 ppm¹⁰. Therefore, detecting ethanol gas is crucial not only for preventing fires due to its volatility and flammability but also for protecting individuals from harmful exposure. Additionally, ethanol detection is important in applications such as distinguishing food spoilage^{5,11} and monitoring drunk driving incidents^{12,13}.

One of the approaches to detect ethanol vapor is using metal oxides as chemiresistive materials, owing to their high sensitivity and cost-effectiveness¹⁴. Among various metal oxides, tin dioxide(SnO_2) stands out as a particularly promising candidate due to its direct bandgap (3.6 eV)¹⁵, high conductivity, chemical stability^{16,17}, and strong oxygen adsorption capability¹⁸, which facilitate redox reactions with gaseous species in air. This makes SnO_2 not only suitable for gas sensor applications but also valuable in other fields such as photocatalysts¹⁹, ion

Correspondence: Seong-Ju Hwang (hwangsj@yonsei.ac.kr) or Jongbaeg Kim (kimjb@yonsei.ac.kr)

¹School of Mechanical Engineering, Yonsei University, 50 Yonsei-ro, Seodaemun-gu, Seoul 03722, Republic of Korea

²Department of Precision Mechanical Engineering and Convergence Research Center of Mechanical and Chemical Engineering (CRCMCE), Kyungpook National University, 2559 Gyeongsang-daero, Sangju, Gyeongbuk 37224, Republic of Korea

Full list of author information is available at the end of the article

These authors contributed equally: Wonkeun Park, Yunsung Kang, Xiaoyan Jin

battery anodes²⁰, photovoltaics²¹, and energy storage devices²². Consequently, numerous SnO_2 -based gas sensors have been developed in various nanostructured morphologies, including thin films^{23–25}, nanoparticles^{26–28}, hollow and solid nanospheres^{29–31}, nanowires^{32–34}, and nanosheets^{35–37}. However, despite these extensive efforts, achieving high sensitivity and selectivity for low-concentration ethanol remains an ongoing challenge.

A promising strategy for enhancing gas sensor performance involves forming heterojunctions using functionalization materials^{5,10,24,30}. Ruthenium dioxide (RuO_2) nanosheets, which have primarily been explored for applications in oxygen evolution reaction (OER) catalysts^{38,39} and supercapacitors^{40,41}, remain underexplored in the field of gas sensors. However, due to its OER catalytic electrochemical behavior and high surface-to-volume ratio^{38,39,42}, we focused on its potential application as a functionalization material for gas sensors. Therefore, we aimed to present the characteristics of RuO_2 nanosheets as a catalyst in chemiresistive gas sensors for the first time. We selected ethanol as the target gas because RuO_2 catalysts are known to be effective for oxidizing ethanol even at ambient temperatures⁴³.

Beyond its inherent catalytic properties, RuO_2 provides two critical sensitization effects for the SnO_2 thin film: electronic and chemical sensitization. First, for electronic sensitization, the difference in Fermi energy levels between SnO_2 and RuO_2 induces electron transfer from SnO_2 to RuO_2 , forming a thicker electron depletion layer at the heterojunction interface⁴⁴. This charge transfer, confirmed by the higher baseline resistance of the functionalized sensor in air, enables a more sensitive change in resistance by maximizing the variation in the depletion layer thickness when exposed to ethanol. Second, for chemical sensitization, the exceptional OER catalytic properties of RuO_2 enhance surface reactions by facilitating electron transfer and improving the adsorption/desorption of reactive oxygen species, which are critical to the ethanol detection mechanism. Furthermore, RuO_2 decoration can improve humidity resistance, stemming from the direct formation of a hydrophobic layer or accelerated dissociation of water molecules⁴⁵. These characteristics are particularly suitable for an ethanol sensor intended for practical applications like monitoring breath alcohol concentration. Consequently, RuO_2 nanosheets hold significant potential to improve the performance of ethanol gas sensors, particularly in applications demanding high sensitivity and selectivity. However, to the best of our knowledge, RuO_2 nanosheets have never been used as functionalization materials for gas sensors.

Building upon our previous study that first reported the functionalization of gas sensors using RuO_2 nanosheets⁴⁶,

we fabricated a RuO_2 nanosheets-functionalized SnO_2 thin-film gas sensor integrated with a microheater in a suspended structure. This approach demonstrated high sensitivity, selectivity, reliability, miniaturization, low cost, and low power operation for ethanol gas detection. Here, we present the ethanol gas sensing characteristics of RuO_2 nanosheets-functionalized SnO_2 thin films. The RuO_2 nanosheets enhance the sensitivity of SnO_2 thin films compared to pristine SnO_2 thin films. Additionally, we investigated the gas sensor's response to ethanol as a function of the operating temperature of a microheater. The suspended structure of the sensor platform, which incorporates a microheater, minimizes heat dissipation and enables power consumption below 30 mW during continuous operation. The fabricated sensor demonstrated sensitive detection of ethanol, ranging from a few ppm to ppb levels under experimental conditions. We further achieved a highly competitive limit of detection of ~ 5 ppb, positioning our work among the most sensitive chemiresistive ethanol sensors reported to date. The influence of humidity, selectivity, and long-term stability were also examined. Additionally, the feasibility of this sensor for real-time breath alcohol detection was also demonstrated.

Results and discussion

Sensor platform design and RuO_2 nanosheets characterization

Figure 1a illustrates the schematic design of the fabricated gas sensor platform ($2.25 \times 2.25 \text{ mm}^2$). Figure 1b presents an SEM image of the fabricated gas sensor, in which the RuO_2 nanosheets-functionalized SnO_2 thin film electrically bridges the initially insulated sensor electrodes. This suspended structure minimized heat dissipation to the substrate, enabling the sensor to operate at low power. The synthetic route that yields the monolayer RuO_2 nanosheets is summarized in Fig. 2a. The effective exfoliation into monolayered 2D RuO_2 nanosheets was confirmed by scanning transmission electron microscopy image, which showed a 2D sheet-like morphology with faint contrast (Fig. 2b). Furthermore, atomic force microscopy revealed a very small sub-nanometer level thickness and a much larger lateral size of several hundred nanometers, as shown in Fig. 2c. Although the exfoliation into monolayered RuO_2 nanosheets prevented the observation of well-defined X-ray diffraction peaks of RuO_2 phase, the retention of RuO_2 lattice after the exfoliation process was evidenced by Ru K-edge extended X-ray absorption fine structure (EXAFS) analysis showing the typical Fourier-transformed (FT) feature of layered RuO_2 phase, see Fig. 2d⁴⁷. Combined characterization results clearly demonstrated that the monolayered RuO_2 nanosheets were successfully synthesized. Details of sensor fabrication, RuO_2 synthesis and test conditions are

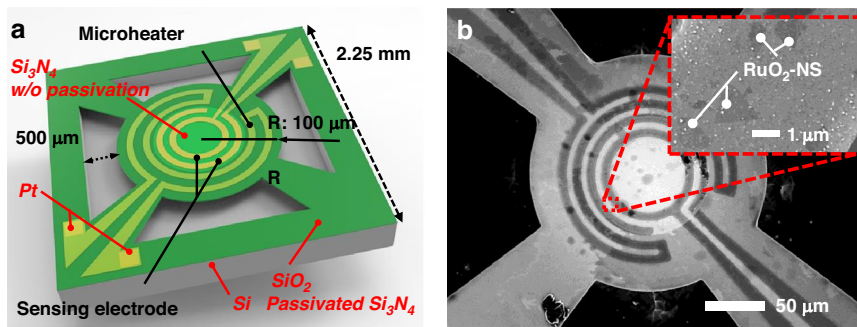


Fig. 1 Structure of the fabricated RuO₂ nanosheets-functionalized SnO₂ thin-film gas sensor. **a** Schematic of the fabricated sensor platform ($2.25 \times 2.25 \text{ mm}^2$). The sensor platform was manufactured through a batch fabrication process, including chemical vapor deposition, e-beam evaporation, inductively coupled plasma etching, photolithography, and silicon wet-etching steps to form a suspended structure. **b** SEM image of the fabricated RuO₂ nanosheets-functionalized SnO₂ thin-film ethanol gas sensor showing the RuO₂ nanosheets coated SnO₂ thin-film surface. RuO₂ nanosheets-functionalized SnO₂ thin film electrically connects the initially insulated sensor electrodes

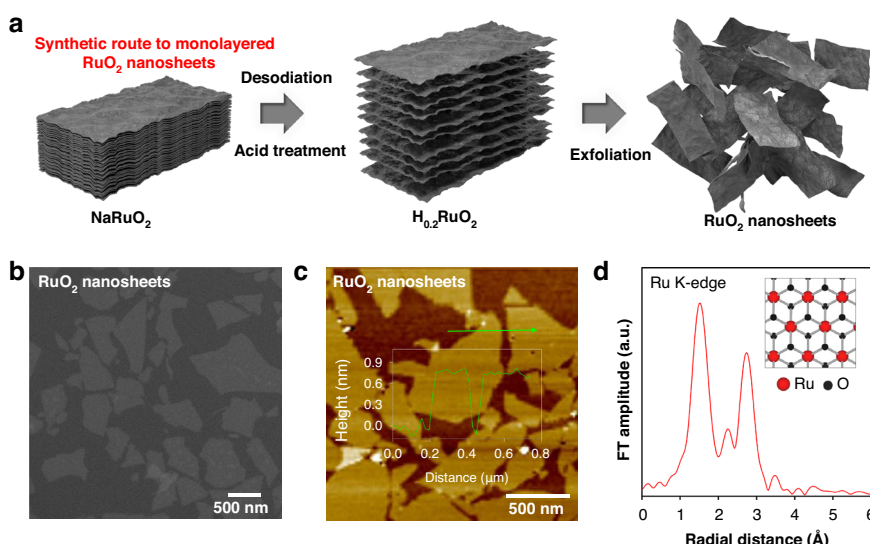


Fig. 2 Synthesis and material characterization of the exfoliated RuO₂ nanosheets. **a** Synthetic route to exfoliated RuO₂ nanosheets. **b** Scanning transmission electron microscopy (STEM) image, **c** atomic force microscopy (AFM) image and height profile (inset), and **d** Ru K-edge extended X-ray absorption fine structure (EXAFS) spectrum and crystal structure of layered RuO₂ (inset)

provided in the “Experimental” section. With the platform architecture established, we next evaluate its gas sensing characteristics.

Comprehensive ethanol gas sensing characteristics

Figure 3a illustrates the sensor responses of SnO₂ thin films before and after RuO₂ nanosheets functionalization. The sensor response is defined as $R_{\text{air}}/R_{\text{gas}}$, where R_{air} and R_{gas} represent the resistance in ambient air and during the exposure to ethanol, respectively, recognizing that ethanol behaves as a reducing gas. In this study, three different sensors were tested to obtain error bars that indicate the response variation. The average response of pristine SnO₂ thin film to 10 ppm ethanol is 3.11. However, after RuO₂

nanosheets functionalization, the average response to 10 ppm ethanol increased to 10.47. This result shows the superiority of RuO₂ nanosheets functionalization by showing that it increased the sensor’s sensitivity to ethanol gas by more than three times compared to pristine SnO₂ thin films. This improvement was further validated by examining the transient response upon exposure to 10 ppm ethanol before and after RuO₂ nanosheets functionalization, as depicted in Fig. 3b.

The transient response in Fig. 3b shows an incomplete recovery curve. It should be noted that the measurement for this initial test was concluded before the baseline was fully restored due to a shorter set duration, not a fundamental limitation of the sensor. The sensor’s ability to

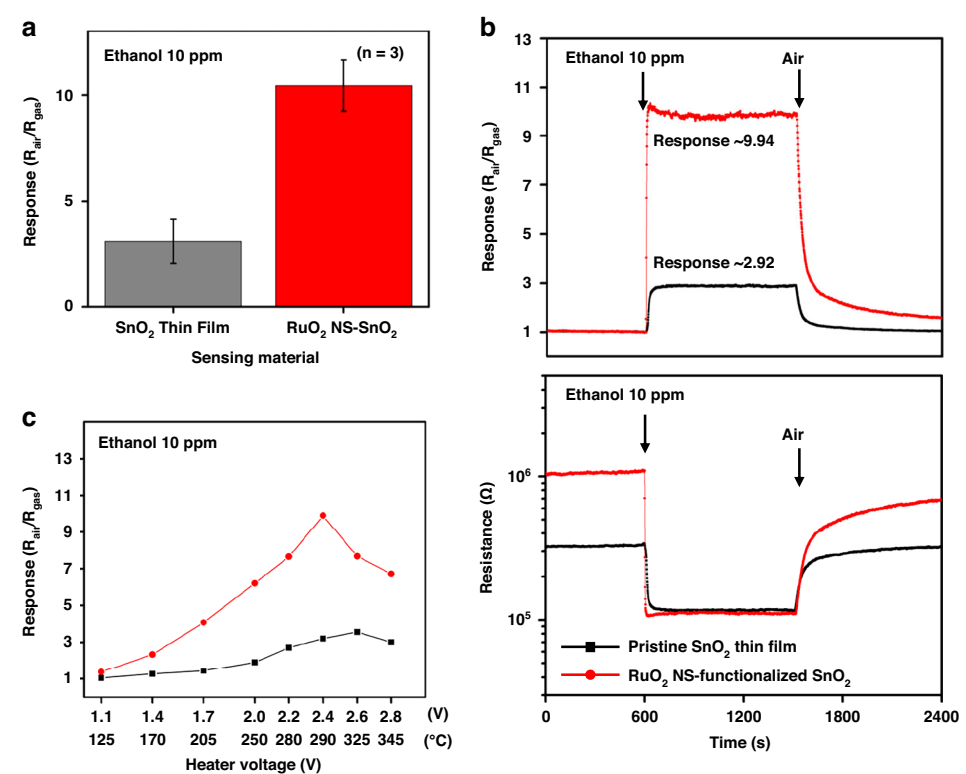


Fig. 3 Ethanol gas sensing performance of the pristine and RuO₂ nanosheets-functionalized SnO₂ thin-film sensors. a Response (R_{air}/R_{gas}) of pristine SnO₂ thin film before and after RuO₂ nanosheets-functionalization to 10 ppm ethanol. Three different sensors were tested to determine the range, which is represented by the error bars. **b** Transient response upon exposure to 10 ppm ethanol before and after RuO₂ nanosheets functionalization. **c** The response of the functionalized sensor to 10 ppm ethanol was evaluated as a function of the applied heater voltage (operating temperature). The fabricated sensor shows the maximum response at a heater voltage of 2.4 V (operating temperature of 290 °C)

fully recover was confirmed in a separate, extended measurement (Fig. S1), which revealed a 90% recovery time (t_{90}) of 224.9 s. While complete, this natural recovery process is relatively slow, which could limit applications requiring rapid measurements.

To address this, we investigated a practical method to accelerate recovery by applying a temporary overheating pulse. A systematic study was conducted by applying a 2.8 V heating pulse (~345 °C) for various durations immediately after ethanol exposure, with the detailed results presented in Fig. S2. As summarized in Fig. S2c, this method is highly effective, but a trade-off between recovery speed and baseline stability was observed, as longer pulses induced greater baseline noise due to likely thermal degradation. A pulse duration of 30 s was identified as the optimal condition, dramatically reducing the recovery time by ~60.8% (from 199.4 s to 78.1 s) without excessively compromising baseline stability. This result demonstrates a highly effective strategy for enhancing the sensor's dynamic performance for practical applications.

Following this, to ensure the practical applicability of the sensor, evaluating the device-to-device reproducibility is crucial, particularly as the RuO₂ nanosheets were

deposited via manual drop-casting, a method that can introduce variability. To address this, we fabricated five independent sensors using the identical process and measured their dynamic responses to 10 ppm ethanol, as shown in Fig. S3. Despite the manual deposition, all five sensors exhibit highly similar response levels and dynamic behavior, visually confirming the reliability of our fabrication method. To quantify this consistency, we analyzed the baseline resistance in air (R_{air}) for the five functionalized sensors, which yielded an average of 0.979 MΩ with a standard deviation of 0.069 MΩ (a relative standard deviation of ~7.1%). While manual drop-casting is a source of minor variation, these results demonstrate robust and acceptable reproducibility for practical use. For future work, coating uniformity can be further enhanced by employing advanced deposition techniques such as dielectrophoretic alignment⁴⁸, controlling the drying environment^{49,50}, or adjusting the Marangoni force⁵¹, which will be subjects of our subsequent research.

Figure 3c presents the sensor response to 10 ppm ethanol as a function of the applied heater voltage, which dictates the average operating temperature. The temperature values were obtained following the methodology

detailed in our former work¹, utilizing the same sensor platform design and fabrication process. Consequently, heater voltages of 1.1, 1.4, 1.7, 2.0, 2.2, 2.4, 2.6, and 2.8 V correspond to average operating temperatures of 125, 170, 205, 250, 280, 290, 325, and 345 °C, respectively. As illustrated in Fig. 3c, the pristine SnO_2 thin film demonstrated an enhanced response at all applied heater voltages after functionalization with RuO_2 nanosheets. Notably, the pristine SnO_2 thin film exhibited its highest response at 2.6 V (i.e., the operating temperature of 325 °C), whereas the RuO_2 nanosheets-functionalized SnO_2 thin-film sensor showed its maximum response at 2.4 V—the optimal operating temperature of 290 °C. This phenomenon of having an optimal operating temperature is well-documented in metal oxide-based gas sensors, where the desorption rate of adsorbed gas molecules surpasses the adsorption rate as the temperature rises, thus leading to an optimal operating temperature⁵². Furthermore, the change in the optimal operating temperature brought about by RuO_2 nanosheets functionalization supports the idea that RuO_2 nanosheets act as a chemical sensitizer, promoting the reaction between oxygen ions adsorbed on the SnO_2 thin film and ethanol gas.

In addition to the operating temperature, the quantity of the functionalization material is another critical parameter that significantly affects sensor performance. To justify the amount of RuO_2 used, we performed a systematic study on the effect of varying the RuO_2 loading levels, with the results presented in the Supplementary Information, Fig. S4. We prepared sensors with one, two, and three drop-casting cycles (corresponding to approximately 2.1, 4.2, and 6.3 ng of RuO_2). As shown in Fig. S4a, the sensor response to 10 ppm ethanol was measured across various operating temperatures for each loading condition. The response peaks with two drop-casting cycles, particularly at the optimal temperature of 290 °C. When the loading was further increased to three cycles, the sensitivity began to decrease, confirming that two drops is the optimal amount for maximizing the sensor response. This decline is attributed to two primary factors: excessive RuO_2 nanosheets can lead to agglomeration, which reduces the effective surface area for gas reactions, and an overly dense layer can act as a physical barrier, hindering the diffusion of target gas molecules to the sensing surface^{53,54}.

Furthermore, we investigated the effect of RuO_2 loading on baseline stability (Fig. S4b). While the baseline resistance (R_{air}) increases with higher loading, the baseline stability degrades, as evidenced by larger noise fluctuations. This can be attributed to two complementary factors. First, from an electrical perspective, a higher baseline resistance leads to larger absolute resistance fluctuations for a given level of inherent current noise⁵⁵. Second, from a material perspective, while RuO_2 nanosheets create the

electron depletion layer that enhances sensitivity, their high-surface-area nature also introduces a higher density of electronically unstable surface sites (e.g., defects and edges), which can increase baseline noise through dynamic charge carrier fluctuations⁵⁶. This creates a beneficial trade-off between sensitivity and stability up to the optimal loading point⁵⁷. Beyond this point, however, the relationship becomes detrimental; further increasing the loading to three drops not only worsens baseline stability but also decreases sensitivity due to overloading effects like nanosheet agglomeration and gas diffusion hindrance. Therefore, the two-drop condition represents the true optimum, maximizing the catalytic benefits for sensitivity without introducing the poor stability and detrimental effects associated with overloading.

Figure 4a illustrates the transient response of the sensor when exposed to ethanol concentrations ranging from 10 down to 1 ppm. Specifically, the measured responses at 10, 5, 2.5, and 1 ppm are 9.96, 7.99, 4.71, and 3.78, respectively, confirming the expected trend of increasing sensor response with higher concentrations. Figure 4b displays the sensor's behavior in the ppb range (20, 10, and 5 ppb), where the responses are 1.046, 1.019, and 1.012, respectively. The inset in Fig. 4b provides an enlarged view of the sensor's response at 5 ppb ethanol. To verify that the observable change at 5 ppb originated from ethanol exposure rather than noise, the signal-to-noise ratio (SNR) was calculated following the method described in a previous work⁵⁸. First, the electrical noise (0.315%) was estimated from 100 points at baseline resistance prior to ethanol introduction. Next, $\Delta R/R_b$ was computed, where ΔR denotes the resistance change during exposure, and R_b represents the baseline resistance. Finally, the SNR was obtained by dividing $\Delta R/R_b$ by the electrical noise, yielding 3.81 at 5 ppb ethanol. Although a commonly accepted limit of detection corresponds to an SNR of 3 or greater⁵⁹, these observations remain significant because the SNR value for 5 ppb ethanol exceeds that threshold. Moreover, to the best of our knowledge, there have been no prior reports of chemiresistive sensors that detect ethanol at several ppb levels. To contextualize our sensor's performance within the current state-of-the-art, we compare our findings with previously reported chemiresistive ethanol sensors in Table S1 (SnO_2 -based) and S2 (other material-based). As shown in Table S1, our sensor's measured limit of detection (LoD) of 5 ppb is highly advantageous and represents one of the lowest values reported for SnO_2 -based ethanol sensors.

While a few studies utilizing other materials have reported even lower LoDs^{60–63} (Table S2), our approach maintains significant practical advantages. For instance, many of these sensors^{60–62} were not demonstrated with an integrated microheater, which is crucial for achieving low power consumption in portable, real-world

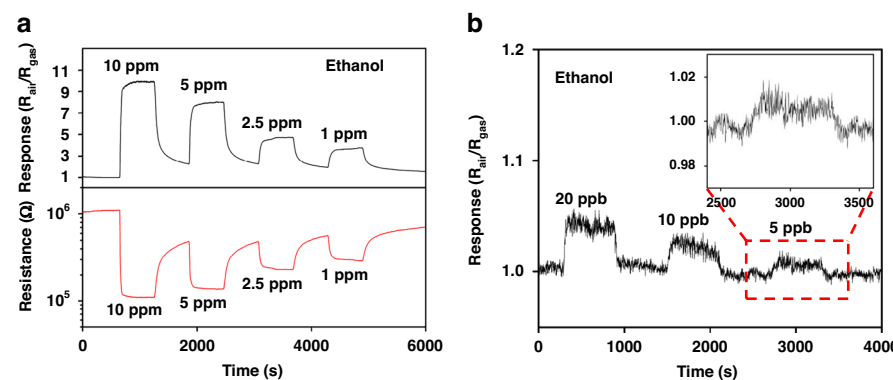


Fig. 4 Transient response of the RuO_2 -functionalized sensor to ethanol concentrations from ppm to ppb levels. **a** Transient response of the fabricated sensor upon exposure to ethanol, ranging from 10 to 1 ppm, and **b** ranging from 20 ppb to 5 ppb. The resistance measured in air (R_{air}) for calculating the sensor response was $1.07 \text{ M}\Omega$. The response was measured using the microheater-integrated sensor positioned in a quartz tube under room temperature. The average operating temperature of the micro heater was 290°C

applications. Another study⁶³ reported a low LoD at room temperature but exhibited a relatively small change in resistance upon ethanol exposure. Therefore, our RuO_2 -functionalized SnO_2 thin-film sensor platform presents a compelling and balanced alternative, offering a rare combination of high sensitivity and a practical, low-power integrated design suitable for real-world deployment.

Figure 5a presents the normalized response of the sensor to 10 ppm ethanol under different humid environments. As detailed in section “Mechanism interpretation of enhanced sensing”, the relative humidity level was regulated using a bubbler-based system, and the relative humidity (RH) values and gases temperatures were monitored using a digital hygrometer. When the relative humidity levels were 5.2, 15.7, 24.9, and 50.5%, the normalized response values were 98.1, 91.0, 83.4, and 76.5%, respectively, indicating a decline in sensor response with increasing humidity.

This trend of decreasing response with increasing humidity is a well-known challenge in metal oxide-based sensors. It is primarily attributed to water molecules interfering with the sensing mechanism by lowering the baseline resistance or hindering the essential chemisorption of oxygen on the sensor surface⁶⁴. However, the functionalization with RuO_2 in our sensor helps to mitigate this effect. The RuO_2 decoration can promote humidity resistance by inducing the formation of a hydrophobic layer or by accelerating the dissociation of water molecules⁴⁵. This improvement is evident when comparing our device to pure SnO_2 -based sensors reported elsewhere, which often exhibit a response decrease of more than 50% at approximately 50% RH^{65–67}. In contrast, our sensor demonstrated a more robust performance, with its response declining by only about 23.5% at 50.5% RH as shown in Fig. 5b.

Nevertheless, to further enhance the sensor’s reliability for real-world applications where humidity varies, several

advanced strategies could be adopted in future work. These include integrating a molecular sieve as a moisture filter⁶⁸, applying a nanoscale moisture-blocking CeO_2 overlayer⁶⁹, developing a humidity compensation model⁷⁰, or using UV illumination⁷¹. For immediate practical implementation, it is advisable to calibrate the sensor response by simultaneously monitoring humidity with a dedicated sensor.

Figure 5b compares the sensor response at 10 ppm for various gases, comparing both the pristine SnO_2 thin film and the RuO_2 nanosheets-functionalized SnO_2 thin film. To quantify the sensor’s selectivity for ethanol, we adopt the selectivity coefficient S_g/S_i , where S_g and S_i denote the responses at the same concentration for the target gas and the interfering gas, respectively^{72–74}. In the pristine SnO_2 thin film, the selectivity coefficients for ethanol against reducing gases such as toluene, acetone, NH_3 , and CO are calculated to be 1.330, 1.198, 1.502, and 2.455, respectively. After functionalizing SnO_2 thin film with RuO_2 nanosheets, these values become 1.598, 2.629, 2.006, and 3.754, indicating enhanced selectivity toward ethanol. This improvement is visually presented in Fig. 5b, where the sensor exhibits a markedly stronger response to ethanol than to other interfering gases. As mentioned in the introduction, one reason for this improvement is that ethanol readily adsorbs onto the oxygen vacancies of RuO_2 , as observed in oxidation catalyst studies^{43,75}, undergoing relatively straightforward oxidation reactions (e.g., forming acetaldehyde or acetic acid) and thus supplying electrons. By contrast, gases such as toluene and acetone have larger molecular sizes and more complex oxidation pathways⁷⁶, while ammonia (NH_3) and carbon monoxide (CO), despite their smaller size, can follow various oxidation mechanisms that do not selectively interact with RuO_2 , which is inferred from a prior study on oxidation catalyst⁷⁷.

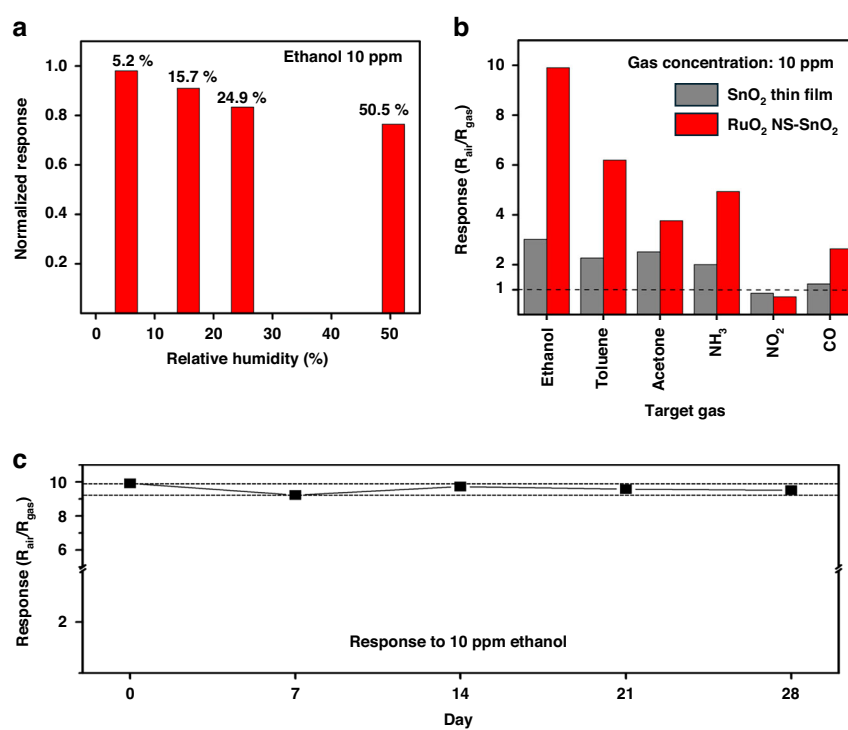


Fig. 5 Selectivity, humidity resistance, and long-term stability of the RuO₂-functionalized sensor. **a** Normalized response of the sensor to 10 ppm ethanol under varying relative humidity conditions. During the humidity-controlled experiments, the ambient temperature inside the quartz tube was $21.2 \pm 1.0^\circ\text{C}$. **b** Sensor responses to various gases, including toluene, acetone, NH₃, NO₂, and CO, all at a concentration of 10 ppm. **c** Long-term stability of the sensor. The experiments were conducted at 7-day intervals. All experiments in (a–c) were performed using the microheater-integrated sensor positioned in a quartz tube at room temperature. The average operating temperature of the micro heater in all experiments was 290 °C

Accordingly, these results suggest that RuO₂ nanosheets function as chemical sensitizers, facilitating targeted reactions between the adsorbed oxygen ions on the SnO₂ surface and ethanol. Although the sensor also responds to nitrogen dioxide (NO₂), it can still be clearly distinguished from reducing gases—including ethanol—because NO₂, a potent oxidizing gas, decreases the sensor's resistance, thereby yielding a response ratio below 1, as observed in Fig. 5b.

While the functionalization with RuO₂ nanosheets demonstrated a clear enhancement in selectivity for ethanol over the tested interfering gases, achieving high specificity remains a critical challenge for deployment in complex real-world environments. To address this limitation, a promising future strategy involves developing a sensor array combined with advanced signal processing.

This approach would utilize an array of sensors, each employing the same SnO₂ thin-film channel but functionalized with different materials known to be effective for ethanol detection, such as gold (Au)⁷⁸, silver (Ag)⁷⁹, or lead oxide (PbO)⁸⁰. Each target gas would then generate a unique response pattern, or “fingerprint,” across the differently functionalized sensors in the array. These complex, high-dimensional signals could be analyzed using

pattern recognition algorithms to distinguish ethanol with high accuracy. For this purpose, techniques such as Principal Component Analysis⁸¹, or more advanced deep learning models like Convolutional Neural Networks⁸² and Recurrent Neural Networks⁸³, have proven effective. This combination of a multi-sensor hardware platform and sophisticated data analysis represents a robust pathway to significantly improve selectivity for practical applications.

To assess the long-term stability of the sensor, experiments were conducted at predetermined intervals, and the outcomes are illustrated in Fig. 5c. Although the response to 10 ppm ethanol decreased slightly over time, the average sensor response over a 28-day period remained at 9.59, with all data points falling within $\pm 3.7\%$ of this mean value. Consequently, the sensor demonstrated robust long-term stability.

In addition to long-term stability and device-to-device reproducibility, the sensor's operational repeatability under frequent cycling is critical for continuous monitoring applications. To evaluate this, we subjected the sensor to 20 consecutive cycles of 10 ppm ethanol exposure over 13.5 h (Fig. S5). The sensor exhibited excellent repeatability, maintaining a highly stable baseline and

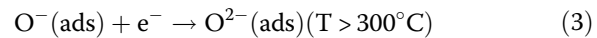
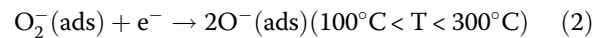
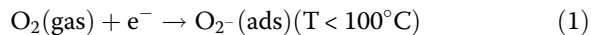
consistent response amplitude across all cycles, with no discernible signal drift. Quantitatively, the average response over the 20 cycles was 9.738 with a standard deviation of 0.046, corresponding to a relative standard deviation of only 0.47%. This high repeatability, combined with the robust 28-day stability shown in Fig. 5c, underscores the sensor's reliability for practical, long-term operation.

However, for applications requiring high-throughput performance, the slow natural recovery time remains a practical challenge. To address this, we propose a two-mode operational strategy utilizing a thermal reset (or overheating) pulse. This method involves operating in a "Sensing Mode" at the optimal temperature (290 °C) for maximum sensitivity, followed by a brief "Recovery Mode" where a high-temperature pulse is applied to accelerate the desorption of residual molecules and rapidly reset the baseline. This temperature-swing approach leverages the sensor's high sensitivity while overcoming the limitation of slow recovery. We have experimentally validated this strategy and optimized the overheating pulse conditions, with the results presented in Supplementary Information (Fig. S2). This protocol enables the sensor to be used in applications requiring reliable, high-throughput performance.

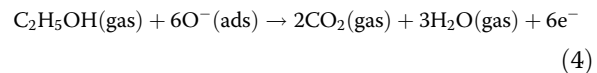
Mechanism interpretation of enhanced sensing

To understand the sensing mechanism, we considered the electronic interactions between SnO_2 thin film and RuO_2 nanosheets.

The fundamental sensing principle of an n-type SnO_2 semiconductor is based on the modulation of its surface resistance by ambient oxygen⁵⁴. When exposed to air, oxygen molecules adsorb onto the SnO_2 surface and capture electrons from its conduction band, forming negatively charged oxygen ions (e.g., O_2^- , O^- , O^{2-})⁷⁹. The specific reactions are temperature-dependent:



Given our primary operating temperature of 290 °C, singly ionized atomic oxygen, O^- (ads), is the dominant reactive species⁷⁹. This electron capture process creates an electron depletion layer on the SnO_2 surface, as illustrated for the pristine film in Fig. 6b, thereby increasing its baseline resistance. When exposed to ethanol ($\text{C}_2\text{H}_5\text{OH}$), the gas molecules react with these surface oxygen ions, releasing the trapped electrons back to SnO_2 's conduction band. This narrows the electron depletion layer and decreases the sensor resistance⁸⁴, according to the overall reaction:



The superior performance of the RuO_2 -functionalized sensor is rooted in the powerful synergy of chemical and electronic sensitization.

First, chemical sensitization is driven by the potent catalytic nature of the RuO_2 nanosheets. Their high surface-to-volume ratio provides an abundance of active sites for reaction, and RuO_2 is known to be an excellent catalyst for ethanol oxidation⁴³. This catalytic action is further amplified by a "spill-over" effect, where partially oxidized ethanol intermediates migrate from the RuO_2 catalyst to the adjacent SnO_2 surface, maximizing the reaction efficiency⁸⁵. This enhanced catalytic activity is experimentally confirmed by the lower optimal operating temperature of the functionalized sensor (Fig. 3c).

Second, electronic sensitization arises from the band structure alignment at the $\text{RuO}_2/\text{SnO}_2$ heterojunction. As shown in the band diagram in Fig. 6a, the work function of RuO_2 is greater than that of SnO_2 , which induces a

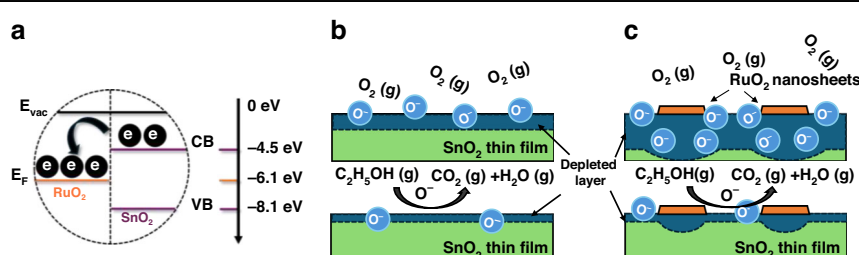


Fig. 6 Proposed mechanism for the enhanced ethanol sensing performance of the RuO_2 -functionalized sensor. **a** Band structure diagram of RuO_2 nanosheets-functionalized SnO_2 thin film. The work function values used for this diagram were adapted from references^{93,94}. Schematic illustration of the ethanol sensing principle in **b** pristine SnO_2 thin film and **c** RuO_2 nanosheets-functionalized SnO_2 thin film at primary operating temperature of 290 °C

spontaneous transfer of electrons from SnO_2 to RuO_2 until their Fermi levels align. This charge transfer significantly expands the initial electron depletion layer at the interface, as conceptually depicted in Fig. 6c. The formation of this wider depletion layer is evidenced by the higher baseline resistance of the functionalized sensor in air (Fig. 3b). Consequently, the reaction with ethanol causes a larger absolute change in the depletion layer width, resulting in a greatly amplified electronic signal.

In summary, the combination of enhanced reaction kinetics (chemical sensitization) and an amplified signal transduction mechanism (electronic sensitization) ensures that reaction (4) occurs more vigorously and is detected more effectively, leading to the outstanding sensitivity of the proposed sensor.

Real-time breath alcohol monitoring application

Accurately monitoring breath alcohol concentration (BrAC) in real-time is essential for applications such as alcohol metabolism assessment and drunk driving prevention. To address this need, we tested an ethanol sensor capable of real-time BrAC detection using the set-up shown in Fig. 7a (protocol details in the “Experimental” section). While the commercial breathalyzer uses a bulkier electrochemical sensing module, our RuO_2 nanosheets-functionalized SnO_2 thin-film sensor offers a

more compact structure, lower power consumption, and comparable performance under real-world conditions.

Initially, both the reference and sensor measurements showed no significant response, as ethanol absorption into the bloodstream required time. Around 20 min after the first intake, as alcohol metabolism commenced, BrAC levels began to rise gradually with each beer intake. Since exhaled breath ethanol originates from the bloodstream via gas exchange in the lungs, BrAC is known to exhibit a linear correlation with blood alcohol concentration (BAC)^{86,87}, making it a reliable non-invasive indicator of BAC levels. As illustrated in Fig. 7b, exhaled ethanol levels increased progressively with each beer intake. The recorded signals demonstrated a strong correlation between breath ethanol levels and cumulative alcohol intake. Additionally, the system effectively captured transient spikes in exhaled ethanol concentration, which are typically attributed to residual alcohol evaporation from the esophagus. The results demonstrated that the sensor successfully distinguished between different BrAC levels, supporting its potential use in breath monitoring applications.

A key challenge for practical BrAC detection is ensuring measurement reproducibility. The measured relative humidity of exhaled breath, for instance, has been reported to vary widely from 40% to over 90% depending

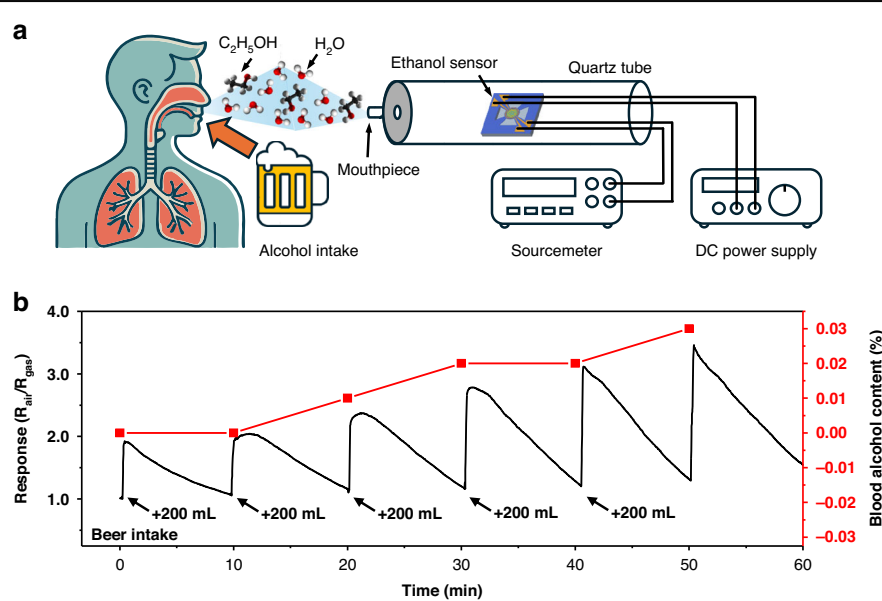


Fig. 7 Real-time monitoring of exhaled breath ethanol concentration using the sensor. **a** Schematic illustration of the experimental setup. The subject consumed 200 mL of beer every 10 min, with BrAC measurements taken prior to each intake. Breath ethanol concentration was measured using two devices: a commercial breathalyzer (Alcoscan AL8800, Sentech Korea Corp.) as a reference, and the developed ethanol sensor integrated with a measurement system. **b** BrAC response recorded over time. The developed ethanol sensor demonstrated a strong correlation with the reference breathalyzer, effectively tracking changes in breath ethanol concentration. The sensor successfully captured transient ethanol spikes and exhibited a rapid response to alcohol intake, confirming its potential for real-time breath alcohol monitoring applications

on the measurement conditions⁸⁸. Significantly, this wide variation was observed in a study using an open-ended device where exhaled breath was allowed to mix with ambient room air before reaching the sensor. This demonstrates how the measurement setup itself can introduce uncontrolled variables, leading to inconsistent results.

In contrast, this issue can be effectively managed through a standardized measurement protocol. In practical use, when a subject exhales immediately into a mouthpiece, the breath reaching the sensor will have a consistent relative humidity approaching 100%^{89–91}. By controlling the exhalation time—as was done in our 4-s protocol—the measurement conditions for each test become highly reproducible. This consistency ensures that the observed trend is reliable, as the primary variable becomes ethanol concentration rather than humidity fluctuations. This suggests that while the absolute response might be affected by humidity, the consistent conditions during measurement will allow for accurate tracking of changes in BrAC. Indeed, despite the high-humidity environment, our sensor effectively captured the increasing trend in BrAC, as shown in Fig. 7b. This successful demonstration underscores its robustness and practical usability for real-world breath monitoring applications. The developed ethanol sensor exhibited high sensitivity and a rapid response time, reinforcing its potential for real-time alcohol metabolism tracking and drunk driving prevention systems.

Conclusions

We have demonstrated an ethanol sensor based on RuO₂ nanosheets-functionalized SnO₂ thin film as a chemiresistive material. The sensor's sensitivity to 10 ppm ethanol increased by more than three times following RuO₂ nanosheets functionalization. We also established that the optimal operating temperature of our sensor is approximately 290 °C using a microheater. The suspended structure of the heater, which minimizes heat loss to the substrate, enabled continuous operation below 30 mW at this temperature. By examining concentrations from 10 ppm down to several ppb, our sensor achieved a significant limit of detection (5 ppb) with an SNR value above 3. In addition, the influence of relative humidity on the sensor's response was also investigated, confirming its humidity-sensitive nature but demonstrating stable performance under controlled conditions. The long-term stability of the sensor was also confirmed through 28-day tests, during which the response to 10 ppm ethanol remained highly consistent. Furthermore, selectivity tests against various gases, including NO₂, toluene, acetone, NH₃, and CO, substantiated that RuO₂ nanosheets act as a chemical sensitizer, enhancing both sensitivity and selectivity to ethanol while maintaining low power

consumption. To validate the sensor's applicability, we tested its performance in real-time breath alcohol monitoring. Controlled alcohol intake experiments confirmed a strong correlation between BrAC measurements and commercial breathalyzers. Despite the high humidity in exhaled breath affecting sensor response, the device successfully tracked BrAC trends, demonstrating its potential for breath alcohol monitoring and diagnostic applications. These results highlight the potential of RuO₂ nanosheets-functionalized SnO₂ thin-film sensors for portable, high-performance ethanol monitoring, with applications extending to safety, environmental, and industrial fields.

Materials and methods

Fabrication of sensor platform and deposition of sensing materials

The platform was manufactured through a batch fabrication process, which included chemical vapor deposition, e-beam evaporation, inductively coupled plasma etching, photolithography, and silicon wet-etching steps. The suspended membrane was formed from silicon nitride deposited on a silicon oxide layer. (Fig. S6) The microheater and sensing electrodes were constructed using 250 nm-thick platinum, arranged in a circular membrane with a radius of 100 μm. The electrode patterns had a width of 7 μm and a spacing of 5 μm. To provide electrical isolation between the microheater and the sensing material, a 200 nm-thick silicon oxide passivation layer was deposited over the microheater electrodes. After preparing the gas sensor platform, the sensing materials were applied onto the sensor electrodes. First, a 50 nm SnO₂ thin film was sputtered using a shadow mask. Then, a colloidal suspension of monolayered RuO₂ nanosheets was manually drop-cast onto the SnO₂ thin film by applying 0.7 μL, followed by drying in a convection oven. Subsequently, an additional 0.7 μL was drop-cast and dried under the same conditions.

Synthesis of RuO₂ nanosheets

The functionalization material, i.e., the RuO₂ nanosheet, was synthesized by the previously reported intercalation-driven exfoliation process of layered a-NaRuO₂ material, as illustrated in Fig. 2a⁹². Typically, the pristine layered a-NaRuO₂ was prepared by conventional solid-state reaction at 900 °C for 12 h using Na₂CO₃, Ru metal, and RuO₂ precursors. The following soft-chemical oxidation using a 1 M Na₂S₂O₈ solution caused partial removal of Na ions, resulting in the increase in the average oxidation state of Ru ions. Protonation of the Na_{0.2}RuO₂ material was conducted by acid-treatment with a 1 M HCl solution for 3 days. The reaction of the protonated Na_{0.2}RuO₂ material with tetrabutylammonium hydroxide (TBA-OH) solution for 10 days produced the colloidal suspension of exfoliated RuO₂ nanosheets. The obtained colloidal

suspension of exfoliated RuO₂ nanosheets after dilution showed a mass concentration of $\sim 3 \mu\text{g mL}^{-1}$.

Evaluation of gas sensor

To assess the ethanol sensing performance of the fabricated sensor, the device was positioned inside a quartz tube. A commercially available ethanol gas mixture (10 ppm ethanol in dry air, Dong-A Specialty Gases, Korea) was used as the source gas. To generate target ethanol concentrations ranging from 10 ppm to 5 ppb, this gas was further diluted with dry air using two mass flow controllers (MFCs). One MFC controlled the flow of the 10 ppm ethanol source gas, and the other regulated the dilution air. By adjusting the flow rate ratio between the two, we accurately controlled the ethanol concentration, while maintaining the total gas flow at 500 sccm. For generating ppb-level concentrations, a precision MFC (maximum 5 sccm range) was used to allow fine control down to 0.01 sccm. The microheater on the sensor platform was powered using a direct current (DC) power supply (E3647A, Agilent) at a constant voltage of 2.4 V during sensor testing under ambient conditions. Different voltages were applied to determine the optimal operating temperature of the microheater experimentally. Because directly measuring the local temperature of the suspended microheater is challenging, we estimated the operating temperature at each voltage using the same RTD-based calibration method reported in our previous work¹. Especially, at 2.4 V, the calibrated temperature was approximately 290 °C, with a corresponding power consumption of 28.8 mW. Such low power consumption at a high operating temperature can be credited to the suspended structure of the sensor platform. To monitor the sensor's response, a voltage of 0.01 V was supplied using a computer-controlled source meter (Keithley 2400), and the corresponding current was measured simultaneously.

To evaluate the sensor's response under different humidity conditions, we used a humidity control setup in which dry air was bubbled through deionized water using a gas-washing bottle. The resulting humidified air stream was then mixed with dry air using two additional MFCs to achieve desired relative humidity (RH) levels. The RH and temperature inside the quartz tube were continuously monitored using a digital hygrometer probe (HQ210, KIMO Instruments). All humidity tests were performed at room temperature (21.2 ± 1.0 °C).

Breath alcohol monitoring protocol

The sensor was evaluated using a controlled drinking experiment to validate its performance in practical scenarios. A healthy volunteer (male, 29 years old) consumed 200 mL of beer with 5.3% alcohol by volume every 10 min, with BrAC measurements taken prior to each intake. The breath alcohol test was conducted with informed consent,

and no human biological samples were collected. According to institutional guidelines, this experiment did not require IRB approval. Breath ethanol concentration was measured using both a commercial breathalyzer (Alcoscan AL8800, Sentech Korea Corp.) as a reference and the developed ethanol sensor integrated with a measurement system (Fig. 7a). During each measurement, the subject exhaled for 4 s, following the same procedure for both devices.

Acknowledgements

This work was supported by the National Research Foundation of Korea (NRF) grant funded by the Korea Government (MSIT) (Nos. RS-2023-00208355, RS-2023-00222166, RS-2024-00348205, RS-2024-00457040).

Author details

¹School of Mechanical Engineering, Yonsei University, 50 Yonsei-ro, Seodaemun-gu, Seoul 03722, Republic of Korea. ²Department of Precision Mechanical Engineering and Convergence Research Center of Mechanical and Chemical Engineering (CRCMCE), Kyungpook National University, 2559 Gyeongsang-dae, Sangju, Gyeongbuk 37224, Republic of Korea.

³Department of Applied Chemistry, University of Seoul, 163 Seoulsiripdaero, Dongdaemun-gu, Seoul 02504, Republic of Korea. ⁴Department of Materials and Science and Engineering, Yonsei University, 50 Yonsei-ro, Seodaemun-gu, Seoul 03722, Republic of Korea

Author contributions

W. Park, Y. Kang, and X. Jin contributed equally to this work. Wonkeun Park: Writing—original draft, Writing—review and editing, Visualization, Validation, Methodology, Formal analysis, Data curation, Conceptualization. Yunsung Kang: Writing—review and editing, Validation, Methodology, Formal analysis, Conceptualization. Xiaoyan Jin: Writing—original draft, Data curation, Investigations. Dongseok Lee: Investigation. Seong-Ju Hwang: Writing—review and editing, Writing—original draft, Validation, Supervision, Resources, Project administration, Funding acquisition, Conceptualization. Jongbaeg Kim: Writing—review and editing, Writing—original draft, Validation, Supervision, Resources, Project administration, Methodology, Investigation, Funding acquisition, Conceptualization.

Conflict of interest

The authors declare no competing interests.

Supplementary information The online version contains supplementary material available at <https://doi.org/10.1038/s41378-025-01055-6>.

Received: 2 July 2025 Revised: 21 August 2025 Accepted: 22 August 2025
Published online: 07 November 2025

References

1. Kang, Y., Kim, K., Cho, B., Kwak, Y., & Kim, J. Highly sensitive detection of benzene, toluene, and xylene based on CoPP-functionalized TiO₂ nanoparticles with low power consumption. *ACS Sens.* **5**, 754–763 (2020).
2. Li, X. et al. Adsorption materials for volatile organic compounds (VOCs) and the key factors for VOCs adsorption process: a review. *Sep. Purif. Technol.* **235**, 116213 (2020).
3. Li, Z. et al. Plasma-induced oxygen vacancies enabled ultrathin ZnO films for highly sensitive detection of triethylamine. *J. Hazard. Mater.* **415**, 125757 (2021).
4. Chakraborty, U. et al. A flower-like ZnO–Ag₂O nanocomposite for label and mediator free direct sensing of dinitrotoluene. *RSC Adv.* **10**, 27764–27774 (2020).
5. Wang, P. et al. Cauliflower-shaped Bi₂O₃–ZnO heterojunction with superior sensing performance towards ethanol. *J. Alloy. Compd.* **854**, 157152 (2021).

6. Zhang, Y., Duan, Z., Zou, H. & Ma, M. Fabrication of electrospun LaFeO₃ nanotubes via annealing technique for fast ethanol detection. *Mater. Lett.* **215**, 58–61 (2018).
7. Hu, Z.-D. et al. Cobalt monosulfide nanofibers: ethanol sensing and magnetic properties. *Rare Met.* **40**, 1554–1560 (2021).
8. Mao, J. et al. Highly improved ethanol gas response of n-type α -Fe₂O₃ bunched nanowires sensor with high-valence donor-doping. *J. Alloy. Compd.* **827**, 154248 (2020).
9. Na, C. W., Woo, H.-S., Kim, I.-D. & Lee, J.-H. Selective detection of NO₂ and C₂H₅OH using a Co₃O₄-decorated ZnO nanowire network sensor. *Chem. Commun.* **47**, 5148–5150 (2011).
10. Ding, Q. et al. Enhanced sensing performance of TiO₂/Ag₃V₄O₁₁ nanoheterostructures to ethanol gas. *J. Alloy. Compd.* **811**, 151958 (2019).
11. Luo, J. et al. E-nose system based on Fourier series for gases identification and concentration estimation from food spoilage. *IEEE Sens. J.* **23**, 3342–3351 (2023).
12. Cai, Z. & Park, S. Enhancement mechanisms of ethanol-sensing properties based on Cr₂O₃ nanoparticle-anchored SnO₂ nanowires. *J. Mater. Res. Technol.* **9**, 271–281 (2020).
13. Li, Q. et al. Highly sensitive sensor based on ordered porous ZnO nanosheets for ethanol detecting application. *Sens. Actuators B Chem.* **326**, 128952 (2021).
14. Dharmalingam, G., Sivasubramaniam, R. & Parthiban, S. Quantification of ethanol by metal-oxide-based resistive sensors: a review. *J. Electron. Mater.* **49**, 3009–3024 (2020).
15. Akgul, F. A. et al. Structural and electronic properties of SnO₂. *J. Alloy. Compd.* **579**, 50–56 (2013).
16. Ab Kadir, R. et al. Electrospun granular hollow SnO₂ nanofibers hydrogen gas sensors operating at low temperatures. *J. Phys. Chem. C* **118**, 3129–3139 (2014).
17. Rajeshwaran, P. & Sivarajan, A. Influence of Mn doping on structural, optical and acetone gas sensing properties of SnO₂ nanoparticles by a novel microwave technique. *J. Mater. Sci. Mater. Electron.* **26**, 539–546 (2015).
18. Nascimento, E. P., Firmino, H. C., Neves, G. A. & Menezes, R. R. A review of recent developments in tin dioxide nanostructured materials for gas sensors. *Ceram. Int.* **48**, 7405–7440 (2022).
19. Al-Hamdi, A. M., Rinner, U. & Sillanpää, M. Tin dioxide as a photocatalyst for water treatment: a review. *Process Saf. Environ. Prot.* **107**, 190–205 (2017).
20. Han, S., Jang, B., Kim, T., Oh, S. M. & Hyeon, T. Simple synthesis of hollow tin dioxide microspheres and their application to lithium-ion battery anodes. *Adv. Funct. Mater.* **15**, 1845–1850 (2005).
21. Xiong, L. et al. Review on the application of SnO₂ in perovskite solar cells. *Adv. Funct. Mater.* **28**, 1802757 (2018).
22. Dalapati, G. K. et al. Tin oxide for optoelectronic, photovoltaic and energy storage devices: a review. *J. Mater. Chem. A* **9**, 16621–16684 (2021).
23. AL-Jawad, S. M., Rasheed, M., Ibrahim, I. M., Sabber, A. S. & Eltayf, A. K. Impact of copper doping on nanocrystalline SnO₂ thin films synthesized by sol-gel coating and chemical bath deposition for gas sensor applications. *J. Nano Res.* **84**, 25–40 (2024).
24. Liu, J. et al. Black phosphorus nanodot incorporated tin oxide hollow-spherical heterojunction for enhanced properties of room-temperature gas sensors. *Ceram. Int.* **49**, 8248–8258 (2023).
25. Ramanathan, G., Srinivasan, N. & Murali, K. Detection of H₂S gas sensing performance of sol gel prepared metal oxide (In₂O₃, SnO₂, Sn doped In2O3) thin films. *Mater. Today Proc.* **92**, 1218–1224 (2023).
26. An, D. et al. Synthesis of Sm doped SnO₂ nanoparticles and their ethanol gas traces detection. *Ceram. Int.* **47**, 26501–26510 (2021).
27. Lian, X. et al. Fabrication of Au-decorated SnO₂ nanoparticles with enhanced n-butanol gas sensing properties. *Mater. Sci. Semicond. Process.* **101**, 198–205 (2019).
28. Liu, D. et al. Ag decorated SnO₂ nanoparticles to enhance formaldehyde sensing properties. *J. Phys. Chem. Solids* **124**, 36–43 (2019).
29. Zhang, R., Ma, S., Zhang, J., Wang, B. & Pei, S. Enhanced formaldehyde gas sensing performance based on Bi doped Zn₂SnO₄/SnO₂ porous nanospheres. *J. Alloy. Compd.* **828**, 154408 (2020).
30. Zhang, S., Zhao, L., Huang, B. & Li, X. UV-activated formaldehyde sensing properties of hollow TiO₂@ SnO₂ heterojunctions at room temperature. *Sens. Actuators B Chem.* **319**, 128264 (2020).
31. Zhong, Y. et al. High-response room-temperature NO₂ sensor and ultrafast humidity sensor based on SnO₂ with rich oxygen vacancy. *ACS Appl. Mater. Interfaces* **11**, 13441–13449 (2019).
32. Cai, Z. & Park, S. Synthesis of Pd nanoparticle-decorated SnO₂ nanowires and determination of the optimum quantity of Pd nanoparticles for highly sensitive and selective hydrogen gas sensor. *Sens. Actuators B Chem.* **322**, 128651 (2020).
33. Choi, M. S. et al. Exploration of the use of p-TeO₂-branch/n-SnO₂ core nanowires nanocomposites for gas sensing. *Appl. Surf. Sci.* **484**, 1102–1110 (2019).
34. Kim, J.-H., Mirzaei, A., Kim, H. W. & Kim, S. S. Improving the hydrogen sensing properties of SnO₂ nanowire-based conductometric sensors by Pd-decoration. *Sens. Actuators B Chem.* **285**, 358–367 (2019).
35. Kim, K., Choi, P. G., Itoh, T. & Masuda, Y. Catalyst-free highly sensitive SnO₂ nanosheet gas sensors for parts per billion-level detection of acetone. *ACS Appl. Mater. Interfaces* **12**, 51637–51644 (2020).
36. Xu, R. et al. Ultrathin SnO₂ nanosheets with dominant high-energy {001} facets for low temperature formaldehyde gas sensor. *Sens. Actuators B Chem.* **289**, 186–194 (2019).
37. Zhao, C. et al. Facile synthesis of SnO₂ hierarchical porous nanosheets from graphene oxide sacrificial scaffolds for high-performance gas sensors. *Sens. Actuators B Chem.* **258**, 492–500 (2018).
38. Vignolo-González, H. A. et al. Morphology matters: 0D/2D WO₃ nanoparticle-ruthenium oxide nanosheet composites for enhanced photocatalytic oxygen evolution reaction rates. *Adv. Energy Mater.* **13**, 2203315 (2023).
39. Liu, Y. et al. Construction of Pd-doped RuO₂ nanosheets for efficient and stable acidic water oxidation. *Green. Energy Environ.* **9**, 937–948 (2024).
40. Vijayabala, V., Senthilkumar, N., Nehru, K. & Karvembu, R. Hydrothermal synthesis and characterization of ruthenium oxide nanosheets using polymer additive for supercapacitor applications. *J. Mater. Sci. Mater. Electron.* **29**, 323–330 (2018).
41. Kim, J.-Y. et al. Nanosheet-assembled 3D nanoflowers of ruthenium oxide with superior rate performance for supercapacitor applications. *RSC Adv.* **4**, 16115–16120 (2014).
42. Zhao, Z. L. et al. Boosting the oxygen evolution reaction using defect-rich ultra-thin ruthenium oxide nanosheets in acidic media. *Energy Environ. Sci.* **13**, 5143–5151 (2020).
43. Liu, H. & Iglesia, E. Selective oxidation of methanol and ethanol on supported ruthenium oxide clusters at low temperatures. *J. Phys. Chem. B* **109**, 2155–2163 (2005).
44. Zhu, L.-Y. et al. Advances in noble metal-decorated metal oxide nanomaterials for chemiresistive gas sensors: overview. *Nano Micro Lett.* **15**, 89 (2023).
45. Yang, S., Sun, H., Sun, Z., Wang, H. & Yang, X. RuO₂ sensitized metal organic framework derived In2O3 hollow nanotubes for ultra-sensitive and high-humidity trimethylamine detection. *J. Alloy. Compd.* **1024**, 180255 (2025).
46. Park, W. et al. In Proc. IEEE 37th International Conference on Micro Electro Mechanical Systems (MEMS) 863–866 (IEEE, 2024).
47. Jin, X. et al. Crucial roles of interfacial coupling and oxygen defect in multi-functional 2D inorganic nanosheets. *Nano Energy* **67**, 104192 (2020).
48. Shao, F. et al. NH₃ sensing with self-assembled ZnO-nanowire pH_P sensors in isothermal and temperature-pulsed mode. *Sens. Actuators B Chem.* **226**, 110–117 (2016).
49. Tao, R. et al. Homogeneous surface profiles of inkjet-printed silver nanoparticle films by regulating their drying microenvironment. *J. Phys. Chem. C* **121**, 8992–8998 (2017).
50. Parsa, M., Harmand, S., Sefiane, K., Bigerelle, M. & Deltombe, R. Effect of substrate temperature on pattern formation of nanoparticles from volatile drops. *Langmuir* **31**, 3354–3367 (2015).
51. Pyeon, J., Song, K. M., Jung, Y. S. & Kim, H. Self-induced solutal marangoni flows realize coffee-ring-less quantum dot microarrays with extensive geometric tunability and scalability. *Adv. Sci.* **9**, 2104519 (2022).
52. Bendahan, M., Guerin, J., Boulmani, R. & Aguir, K. WO₃ sensor response according to operating temperature: Experiment and modeling. *Sens. Actuators B Chem.* **124**, 24–29 (2007).
53. Zhu, M. et al. Chemoresistive gas sensors based on noble-metal-decorated metal oxide semiconductors for H₂ detection. *Materials* **18**, 451 (2025).
54. Najafi, P. & Ghaemi, A. Chemiresistor gas sensors: design, challenges, and strategies: a comprehensive review. *Chem. Eng. J.* **498**, 154999 (2024).
55. Horowitz, P., Hill, W. & Robinson, I. *The art of electronics* Vol. 2 (Cambridge University Press, 1989).
56. Zhang, J., Liu, X., Neri, G. & Pinna, N. Nanostructured materials for room-temperature gas sensors. *Adv. Mater.* **28**, 795–831 (2016).
57. Fine, G. F., Cavanagh, L. M., Afonja, A. & Binions, R. Metal oxide semi-conductor gas sensors in environmental monitoring. *Sensors* **10**, 5469–5502 (2010).
58. Kim, S. J. et al. Metallic Ti₃C₂T x MXene gas sensors with ultrahigh signal-to-noise ratio. *ACS Nano* **12**, 986–993 (2018).

59. Currie, L. A. Nomenclature in evaluation of analytical methods including detection and quantification capabilities (IUPAC Recommendations 1995). *Pure Appl. Chem.* **67**, 1699–1723 (1995).
60. Meng, F. et al. Ag-decorated ultra-thin porous single-crystalline ZnO nanosheets prepared by sunlight induced solvent reduction and their highly sensitive detection of ethanol. *Sens. Actuators B Chem.* **209**, 975–982 (2015).
61. Zhao, J. et al. Highly sensitive ethanol sensor based on two-dimensional layered mesoporous In_2O_3 nanosheets. *IEEE Trans. Nanotechnol.* **19**, 486–491 (2020).
62. Abideen, Z. U. et al. Oxygen vacancies engineering in thick semiconductor films via deep ultraviolet photoactivation for selective and sensitive gas sensing. *Adv. Electron. Mater.* **9**, 2200905 (2023).
63. Zhang, D., Cao, Y., Wu, J. & Zhang, X. Tungsten trioxide nanoparticles decorated tungsten disulfide nanoheterojunction for highly sensitive ethanol gas sensing application. *Appl. Surf. Sci.* **503**, 144063 (2020).
64. Wang, C., Yin, L., Zhang, L., Xiang, D. & Gao, R. Metal oxide gas sensors: sensitivity and influencing factors. *Sensors* **10**, 2088–2106 (2010).
65. Suematsu, K., Ma, N., Yuasa, M., Kida, T. & Shimano, K. Surface-modification of SnO_2 nanoparticles by incorporation of Al for the detection of combustible gases in a humid atmosphere. *RSC Adv.* **5**, 86347–86354 (2015).
66. Motsoeneng, R. G., Kortidis, I., Ray, S. S. & Motaung, D. E. Designing SnO_2 nanostructure-based sensors with tailored selectivity toward propanol and ethanol vapors. *ACS Omega* **4**, 13696–13709 (2019).
67. Tian, X. et al. Controllable acid vapor oxidation growth of complex SnO_2 nanostructures for ultrasensitive ethanol sensing. *Ceram. Int.* **48**, 9229–9238 (2022).
68. Liu, W. et al. A highly sensitive and moisture-resistant gas sensor for diabetes diagnosis with Pt@ In_2O_3 nanowires and a molecular sieve for protection. *NPG Asia Mater.* **10**, 293–308 (2018).
69. Li, H.-Y., Lee, C.-S., Kim, D. H. & Lee, J.-H. Flexible room-temperature NH_3 sensor for ultrasensitive, selective, and humidity-independent gas detection. *ACS Appl. Mater. Interfaces* **10**, 27858–27867 (2018).
70. Yan, M. et al. Humidity compensation based on power-law response for MOS sensors to VOCs. *Sens. Actuators B Chem.* **334**, 129601 (2021).
71. Liu, Y. et al. Highly sensitive and humidity-independent ethanol sensors based on In_2O_3 nanoflower/ SnO_2 nanoparticle composites. *RSC Adv.* **5**, 52252–52258 (2015).
72. Gao, H. et al. Highly selective and sensitive xylene gas sensor fabricated from $\text{NiO}/\text{NiCr}_2\text{O}_4$ pp nanoparticles. *Sens. Actuators B Chem.* **284**, 305–315 (2019).
73. Kim, B.-Y. et al. Highly selective xylene sensor based on $\text{NiO}/\text{NiMoO}_4$ nanocomposite hierarchical spheres for indoor air monitoring. *ACS Appl. Mater. Interfaces* **8**, 34603–34611 (2016).
74. Lee, J. et al. Ultra-selective and stable ethylene detection via exsolution of catalytic Ni nanoparticles in chemiresistive gas sensors. *J. Mater. Chem. A* **13**, 4851–4860 (2025).
75. James, D. D., Moghaddam, R. B., Chen, B. & Pickup, P. G. Ruthenium-tin oxide/carbon supported platinum catalysts for electrochemical oxidation of ethanol in direct ethanol fuel cells. *J. Electrochem. Soc.* **165**, F215 (2018).
76. Liu, W., Liu, R. & Zhang, X. Controllable synthesis of 3D hierarchical Co_3O_4 catalysts and their excellent catalytic performance for toluene combustion. *Appl. Surf. Sci.* **507**, 145174 (2020).
77. Huang, Z., Zhao, L., Zhu, J. & He, D. Three-dimensional electrochemical oxidation system with $\text{RuO}_2/\text{IrO}_2/\text{Ti}$ as the anode for ammonia wastewater treatment. *Sustainability* **16**, 1838 (2024).
78. Li, J. et al. Low-temperature and high-sensitivity Au-decorated thin-walled SnO_2 nanotubes sensor for ethanol detection. *Mater. Today Commun.* **37**, 107217 (2023).
79. Dong, J. et al. Enhanced ethanol gas sensing performance of Ag/SnO_2 composites. *Sens. Actuators B: Chem.* **423**, 136721 (2025).
80. Hyun, S. K. et al. Ethanol gas sensing using a networked PbO -decorated SnO_2 nanowires. *Thin Solid Films* **637**, 21–26 (2017).
81. Khan, M. A. H., Thomson, B., Debnath, R., Motayed, A. & Rao, M. V. Nanowire-based sensor array for detection of cross-sensitive gases using PCA and machine learning algorithms. *IEEE Sens. J.* **20**, 6020–6028 (2020).
82. Kang, M. et al. High accuracy real-time multi-gas identification by a batch-uniform gas sensor array and deep learning algorithm. *ACS Sens.* **7**, 430–440 (2022).
83. Wang, Z. et al. Improved deep bidirectional recurrent neural network for learning the cross-sensitivity rules of gas sensor array. *Sens. Actuators B Chem.* **401**, 134996 (2024).
84. Cao, H. et al. Conductometric ethanol gas sensor based on a bilayer film consisting of SnO_2 film and $\text{SnO}_2/\text{ZnSnO}_3$ porous film prepared by magnetron sputtering. *Sens. Actuators B Chem.* **382**, 133562 (2023).
85. Kruefu, V., Wisitsoraat, A., Phokharatkul, D., Tuantranont, A. & Phanichphant, S. Enhancement of p-type gas-sensing performances of NiO nanoparticles prepared by precipitation with RuO_2 impregnation. *Sens. Actuators B Chem.* **236**, 466–473 (2016).
86. Lindberg, L. et al. Breath alcohol concentration determined with a new analyzer using free exhalation predicts almost precisely the arterial blood alcohol concentration. *Forensic Sci. Int.* **168**, 200–207 (2007).
87. Mayer, M. N. & Rafiee, M. Electrocatalytic detection of ethanol and acet-aldehyde by aminoxy radicals: utilizing molecular catalysis for breath analysis. *Analyst* **147**, 3420–3423 (2022).
88. Mansour, E. et al. Measurement of temperature and relative humidity in exhaled breath. *Sens. Actuators B Chem.* **304**, 127371 (2020).
89. Bruderer, T. et al. On-line analysis of exhaled breath: focus review. *Chem. Rev.* **119**, 10803–10828 (2019).
90. Bouverot, P. *Adaptation to Altitude-Hypoxia in Vertebrates* Vol. 16 (Springer Science & Business Media, 2012).
91. Déry, R. Humidity in anaesthesiology IV: determination of the alveolar humidity and temperature in the dog. *Can. Anaesth. Soc. J.* **18**, 145–151 (1971).
92. Fukuda, K. et al. Synthesis of nanosheet crystallites of ruthenate with an α - NaFeO_2 -related structure and its electrochemical supercapacitor property. *Inorg. Chem.* **49**, 4391–4393 (2010).
93. Elumalai, N. K., Vijila, C., Jose, R., Uddin, A. & Ramakrishna, S. Metal oxide semiconducting interfacial layers for photovoltaic and photocatalytic applications. *Mater. Renew. Sustain. Energy* **4**, 1–25 (2015).
94. Uddin, M. T. et al. Preparation of $\text{RuO}_2/\text{TiO}_2$ mesoporous heterostructures and rationalization of their enhanced photocatalytic properties by band alignment investigations. *J. Phys. Chem. C* **117**, 22098–22110 (2013).